The Role of Eddies in the Zonal and Meridional Overturning Circulations of Buoyancy-Forced Basins

SUYASH BIRE[a] AND CHRISTOPHER L.P. WOLFE[b]

[a] *Department of Earth, Atmospheric and Planetary Sciences, Massachusetts Institute of Technology, Cambridge, Massachusetts*
[b] *School of Marine and Atmospheric Sciences, Stony Brook University, State University of New York, Stony Brook, New York*

(Manuscript received 29 January 2020, in final form 17 September 2020)

ABSTRACT: The zonal and meridional overturning circulations of buoyancy-forced basins are studied in an eddy-resolving model. The zonal overturning circulation (ZOC) is driven by the meridional gradient of buoyancy at the surface and stratification at the southern boundary. The ZOC, in turn, produces zonal buoyancy gradients through upwelling and downwelling at the western and eastern boundaries, respectively. The meridional overturning circulation (MOC) is driven by these zonal gradients rather than being directly driven by meridional gradients. Eddies lead to a broadening of the upwelling and downwelling limbs of the ZOC, as well as a decoupling of the locations of vertical and diapycnal transport. This broadening is more prominent on the eastern boundary, where westward-moving eddies transport warm water away from a poleward-flowing eastern boundary current. Most of the diapycnal downwelling occurs in the ''swash zone''—the region where the isopycnals intermittently come in contact with the surface and lose buoyancy to the atmosphere. A scaling for the overturning circulations, which depends on the background stratification and the surface buoyancy gradient, is derived and found to be an excellent fit to the numerical experiments.

KEYWORDS: Ocean; Meridional overturning circulation; Mesoscale processes; Ocean circulation; Ocean dynamics

1. Introduction

Oceanic mesoscale eddies play a crucial role in the climate system, and the role of eddies in the Atlantic meridional overturning circulation (MOC) is well known (Gnanadesikan 1999; Vallis 2000; Wolfe and Cessi 2010; Nikurashin and Vallis 2011; Allison et al. 2011; Mazloff et al. 2013; Jones and Cessi 2016; Ferrari et al. 2017a). In the Antarctic Circumpolar Current, northward Ekman transport due to the surface westerlies is opposed by the southward transport due to eddies. This balance between eddy and Ekman transport—along with diapycnal diffusion, North Atlantic deep-water formation, and interbasin transport—is responsible for setting the depth of the pycnocline throughout the meridional extent of the Atlantic basin (Gnanadesikan 1999; Marshall and Radko 2003, 2006; Wolfe and Cessi 2010; Nikurashin and Vallis 2011, 2012; Cessi and Jones 2017).

The MOC is in thermal wind balance with basin-scale zonal buoyancy gradients (Zhang et al. 1992). These buoyancy gradients cannot come from the large-scale wind and surface buoyancy forcing because they are both largely zonally uniform. These buoyancy gradients are instead established by the zonal overturning circulation (ZOC; Cessi et al. 2010). The ZOC arises in response to meridional gradients in surface buoyancy that drive an eastward flow at the surface which returns westward at intermediate depths. The circulation is closed by upwelling and downwelling boundary layers on the western and eastern boundaries, respectively. In this study we show that while the vertical velocity is concentrated in these narrow boundary layers, the diapycnal transformation required to close the circulation is spread over a much broader area by the effect of the eddies. This effect is especially prominent on the eastern boundary.

Previous studies, mainly concerned with the zonal location of the downwelling branch of the MOC, have shown that downwelling occurs in narrow boundary layers on the eastern boundary. For example, Spall and Pickart (2001) argue that the downwelling limb of the MOC primarily occurs over sloping topography along boundaries rather than in the interior of the basin. Pedlosky (2003) and Spall (2003) show that, in a convectively driven semi-enclosed basins, upwelling or downwelling is found in narrow ''hydrostatic''[1] boundary layers in spite of the heating or cooling being concentrated in the interior. In the hydrostatic layer, vertical buoyancy advection is balanced by horizontal eddy transport and vortex stretching is balanced by viscous dissipation (Barcilon and Pedlosky 1967). The width of the hydrostatic layer scales like

$$\delta_h = \sqrt{\frac{A_h}{K_e}} L_d, \tag{1}$$

where A_h and K_e are the horizontal eddy viscosity and diffusivity, respectively, and L_d is the deformation radius; for realistic parameters, δ_h is very small (less than 10 km). The general consensus of these studies is that the downwelling limbs of the overturning circulation occur in narrow boundary layers on the eastern boundary with widths primarily governed by hydrostatic layer or the bottom slope. Note that Pedlosky and Spall (2005) find that the β effect enhances the role of the western

[1] Note that all models discussed here are hydrostatic. The name ''hydrostatic layer'' is historical and contrasts this boundary layer with an even thinner nonhydrostatic boundary layer that occurs in nonhydrostatic models.

Corresponding author: Suyash Bire, bire@mit.edu

DOI: 10.1175/JPO-D-20-0025.1

boundary at the expense of the eastern boundary, but these conclusions pertain to a regime where both thermal forcing and eddy mixing are weak so the that the flow is largely determined by inviscid Rossby wave dynamics.

Later studies show that—although the downwelling is concentrated in a narrow eastern boundary layer—eddies transport buoyancy from the boundary current toward the west, thereby extending the region over which cooling takes place (e.g., Spall 2010, 2011; Katsman et al. 2018; Georgiou et al. 2019; Brüggemann and Katsman 2019). In these studies, the rate of densification is controlled by the balance between the westward advection of buoyancy by eddies and cooling by the atmosphere. Cessi and Wolfe (2013) examine the eastern boundary circulation in the residual-mean framework and find that diapycnal transformation is decoupled from the downwelling in the narrow eastern boundary layer. Bire and Wolfe (2018) also find that the narrow downwelling layer on the eastern boundary in the Eulerian-mean vertical velocity is nearly adiabatic while diapycnal transformation is extended westward by eddies over a broad region. In this study, we carry out eddy-resolving simulations of buoyancy-driven circulation in a Northern Hemisphere basin to further examine the processes driving the ZOC and the MOC. Comparison of the residual-mean and the Eulerian-mean circulations shows how eddies broaden the diapycnal downwelling limb of the ZOC. The broadening of the downwelling limb of the ZOC is shown to be consistent across a suite of experiments with varying surface forcing and stratification.

The rest of the paper is structured as follows. The numerical experiments and the large-scale circulation are described in sections 2 and 3, respectively. The residual-mean, Eulerian-mean, and eddy-driven components of ZOC and MOC are derived and discussed in section 4. The dynamics driving the ZOC and MOC are described in section 5. In section 6, the eddy-driven component of the residual overturning circulation is shown to be well modeled by thickness diffusion. A scaling theory for the overturning circulation is developed in section 7. Finally, section 8 gives a summary and discussion.

2. Model setup

We use the Modular Ocean Model, version 6 (MOM6), to simulate the circulation in a Northern Hemispheric sector that extends from 10° to 60°N meridionally, from −25° to 0° zonally, and is 3000 m deep. The horizontal resolution is 0.04° × 0.04°. The vertical grid is isopycnal with 30 layers evenly spaced in buoyancy from 0 to 0.03 m s^{-2}. The Laplacian viscosity is 10 m^2 s^{-1} and Smagorinsky biharmonic viscosity, with a coefficient of 0.06 (Griffies and Hallberg 2000), is used to remove gridscale noise.

We make use of the linear equation of state

$$b = \frac{db}{d\theta}(\theta - \theta_{\rm bot}), \tag{2}$$

where

$$\frac{db}{d\theta} = 2 \times 10^{-3}\ {\rm m\,s^{-2}\,K^{-1}} \tag{3}$$

and $\theta_{\rm bot}$ = 5°C in the control case. Forcing is applied at the surface isopycnal layer according to the relation

$$\frac{\partial h}{\partial t} = \frac{w^*}{\Delta\theta'}(T^* - \theta_{\rm surf}), \tag{4}$$

where $\Delta\theta'$ = 0.5°C is the (constant) temperature difference between two successive isopycnals, and $\theta_{\rm surf}$ is the temperature averaged over the upper 20 m. The piston velocity is w^* = 4 m day^{-1}, which corresponds to a bulk heat transfer coefficient of $\lambda \approx 200\ {\rm W\,m^{-2}\,K^{-1}}$ (Haney 1971). This is about 5 times the "typical" value of the bulk transfer coefficient and puts the forcing used in this study closer to the "fixed buoyancy" limit than the "fixed flux" limit. While using a fixed-buoyancy boundary condition is a standard paradigm for studies of the ocean's overturning circulation (e.g., Gnanadesikan 1999; Wolfe and Cessi 2011; Nikurashin and Vallis 2012; Ferrari et al. 2017b), we acknowledge that the scalings derived herein would likely be different if fixed-flux conditions were used instead (Stewart et al. 2014). Extension of the present results to the fixed-flux limit is beyond the scope of this study. We note, however, that reducing the piston velocity by a factor of 4 does not significantly affect the results. The relaxation temperature profile is given by

$$T^* = \begin{cases} T_{\rm max}, & y \le 20°{\rm N}, \\ T_{\rm max} - \dfrac{\Delta T}{20°{\rm N}}(y - 20°{\rm N}), & 20°{\rm N} < y \le 40°{\rm N}, \\ T_{\rm max} - \Delta T, & y > 40°{\rm N}, \end{cases} \tag{5}$$

where $T_{\rm max}$ = 20°C and ΔT can be varied. The control run has ΔT = 10°C and the resulting meridional profile is shown in Fig. 1a.

The region between 10° and 14°N serves as a sponge layer in which the temperature is rapidly relaxed to a vertical profile of temperature that decreases linearly from $T_{\rm max}$ = 20°C at the surface to $T_{\rm bot}$ at $D_{\rm abyss}$. Below $D_{\rm abyss}$, the southern boundary temperature is relaxed to $T_{\rm bot}$ so that $D_{\rm abyss}$ serves as the upper depth of an abyssal layer of constant buoyancy. For the control run, $T_{\rm bot}$ = 5°C and $D_{\rm abyss}$ = 1500 m.

The model is run for ~35 years at a time step of 300 s, whereafter it attains a statistically steady state. The diagnostics presented hereafter are all averaged over 10 years from year 37 to 46. The surface buoyancy gradient, the stratification at the southern boundary, and diapycnal diffusivity are varied in additional numerical experiments, with all the other parameters held fixed. Four additional simulations with varying ΔT, two simulations with varying $T_{\rm bot}$, two with varying $D_{\rm abyss}$, and two with varying diapycnal diffusivity K_D, are also performed. These experiments are listed in Table 1.

3. Description of the circulation

The imposed meridional SST gradient (Fig. 1a) drives a surface eastward flow which turns northward on contact with the eastern boundary as shown schematically in Fig. 1b. This northward current is baroclinically unstable and sheds predominantly warm core eddies. The water transported by these

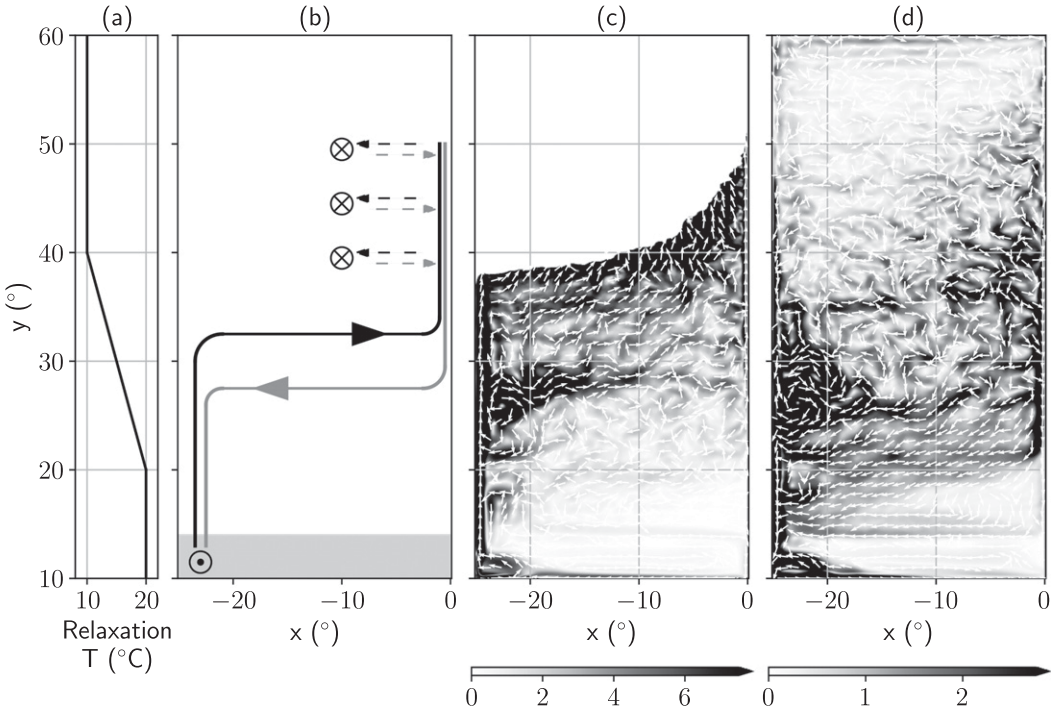

FIG. 1. (a) Meridional profile of relaxation temperature T^* for control run. (b) Schematic of the baroclinic circulation. Pathways in black and gray show surface and deep (~1250 m) circulation, respectively. Dashed lines indicate transport by eddies. Circles with crosses and dots represent diapycnal upwelling and downwelling, respectively. Vertically averaged velocities are shown in (c) the upper 16 layers and (d) between layers 17 and 29. Arrows show direction and shading shows speed (cm s^{-1}). Note that the shading is capped at the 90th percentile to accentuate the arrows.

warm core eddies (dashed black arrows in Fig. 1b) eventually sinks (black circles with crosses in Fig. 1) as the eddies dissipate and their warm cores cool. This downwelled water returns to the eastern boundary (dashed gray arrows in Fig. 1b) and travels south as an eastern boundary undercurrent which then turns westward at around 25°N. This deep westward flow feeds a southward deep western boundary current. The circulation is closed in the southwestern corner of the domain where the deep western boundary current upwells (black circle with dot in Fig. 1b) under the action of strong relaxation in the sponge layer (gray region in Fig. 1b), and feeds into a northward surface western boundary current which turns eastward at approximately 25°N. See Bire and Wolfe (2018) for a more detailed description. Zonal and meridional overturning circulations emerge as a result of the circulation along the black and gray pathways. The upper limb (black pathway) of the overturning cells occupies the upper 16 layers and the lower limb (gray pathway) occupies layers 17–29. Averaged velocities in these two sets of layers show horizontal structure of these pathways (Figs. 1c,d).

TABLE 1. Experiments with varying surface forcing, southern boundary stratification, and diapycnal diffusivity. Experiment 1 is the control.

	ΔT (°C)	Δb (10^{-3} m s^{-2})	θ_{bot} (°C)	D_{abyss} (m)	N (10^{-3} s^{-1})	K_D (10^{-5} m^2 s^{-1})
1	10	2	5	1500	4.4721	10
2	8	1.6	5	1500	4.4721	10
3	9	1.8	5	1500	4.4721	10
4	11	2.2	5	1500	4.4721	10
5	12	2.4	5	1500	4.4721	10
6	10	2	5	1750	4.1404	10
7	10	2	6	1500	4.3205	10
8	10	2	4	1500	4.6188	10
9	10	2	5	1250	4.8990	10
10	10	2	5	1500	4.4721	5
11	10	2	5	1500	4.4721	2.5

The surface forcing causes isopycnals to successively outcrop in the northern part of the basin, as shown in Fig. 2a (y–z plane). In the buoyancy coordinate model used here, buoyancy always monotonically increases upward. As a result, if cold temperatures occur at the surface, say, due to passage of a cold-core eddy, deeper isopycnals are elevated to the surface and all isopycnals warmer than the surface are squeezed to zero thickness at the top. These isopycnals return to their mean positions once the cold-core eddy moves away. The amount of time an isopycnal spends at the surface can be used to define the *swash zone* as the region from the surface to the mean depth of the isopycnal which outcrops at least 1% of the time (Cessi and Wolfe 2013). Note that different isopycnals satisfy this criteria at different locations. The swash zone is at its deepest where the eddy activity is most intense, in our case, around 40°–50°N near the eastern boundary. This also is the region where the maximum diapycnal downwelling takes place (black circles with crosses in Fig. 1b). Although only the surface layer feels the forcing at any instant, over time the surface forcing is felt by the ocean over the depth of the swash zone.

The mean sea surface height, shown in 2b, has an east–west asymmetry that is responsible for maintaining the surface branch of the MOC. The ZOC and MOC, which are discussed in detail in the following section, give an integrated view of the circulation occurring along black and gray pathways.

4. Mean and eddy contributions to the overturning circulations

Residual velocities, which contain contributions from the mean as well as the eddy-induced velocity, provide a more accurate representation of the Lagrangian flow than Eulerian-mean velocities (Andrews and McIntyre 1976). Following De Szoeke and Bennett (1993) and Young (2012), the residual-mean or thickness-weighted average (TWA) of any quantity θ in the isopycnal coordinates $(\tilde{x}, \tilde{y}, \tilde{b}, \tilde{t})$, is indicated by a circumflex and defined by

$$\hat{\theta} = \frac{\overline{\sigma\theta}}{\overline{\sigma}}, \tag{6}$$

where a bar indicates a time average at constant buoyancy, and

$$\sigma \overset{\text{def}}{=} \frac{\partial \zeta}{\partial \tilde{b}}, \tag{7}$$

where ζ is the isopycnal height, represents the differential thickness of isopycnal layers. According to (6) the residual or thickness-weighted average (TWA) velocities are defined by

$$\hat{u} \overset{\text{def}}{=} \frac{\overline{\sigma u}}{\overline{\sigma}}, \tag{8}$$

$$\hat{v} \overset{\text{def}}{=} \frac{\overline{\sigma v}}{\overline{\sigma}}, \tag{9}$$

$$\hat{\varpi} \overset{\text{def}}{=} \frac{\overline{\sigma \varpi}}{\overline{\sigma}}. \tag{10}$$

The zonal and meridional components of horizontal velocity are u and v, respectively, while

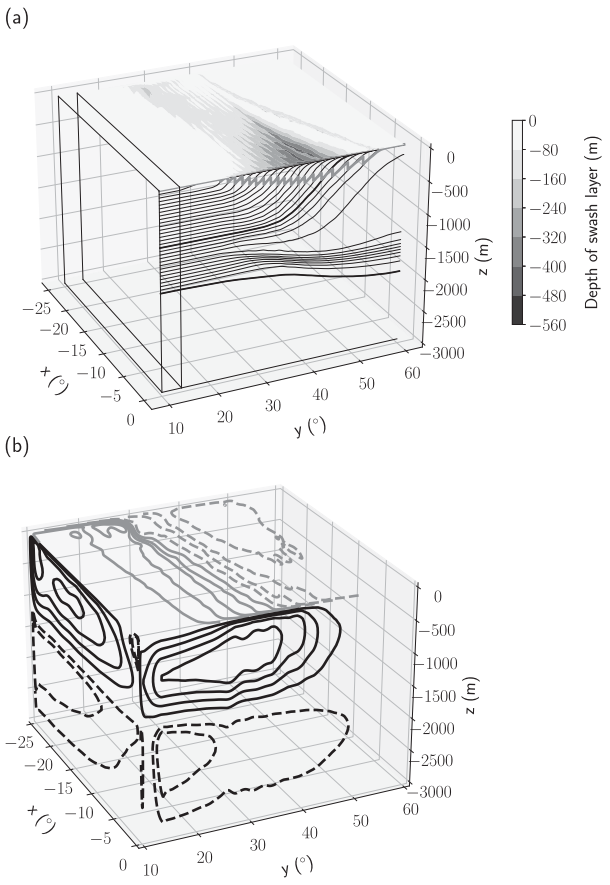

FIG. 2. (a) The depth of the swash zone (m; shading) as a function of x and y is shown in the plan view, while the mean position of the isopycnals at the eastern boundary (black contours) are shown in the y–z plane. Bottom boundaries of 16th and 29th layers are shown by thick black contours. The thick gray contour in the y–z plane represents the bottom boundary of the swash zone at the eastern boundary. Rapid restoration of stratification is achieved in the sponge region sandwiched between the two planes at 10° and 14°N. (b) The mean sea surface height is shown in the plan view. Contours are drawn at −0.4, −0.3, −0.2, −0.1, 0, 0.1, 0.2, 0.3, and 0.4 m. Negative contours are dashed. The residual ZOC and MOC are shown in the x–z plane and y–z plane, respectively. The contours are drawn at −3, −1, 5, 10, 15, and 20 Sv (1 Sv $\equiv 10^6\ \text{m}^3\,\text{s}^{-1}$).

$$\varpi \overset{\text{def}}{=} \frac{Db}{D\tilde{t}} \tag{11}$$

represents a diapycnal "velocity" across isopycnals and is analogous to a vertical velocity seen in conventional height coordinates. The residual thickness flux can be decomposed into mean and eddy components:

$$\overline{\sigma}\hat{u} = \overline{\sigma u} = \overline{\sigma}\,\overline{u} + \overline{\sigma' u'}, \tag{12}$$

$$\overline{\sigma}\hat{v} = \overline{\sigma v} = \overline{\sigma}\,\overline{v} + \overline{\sigma' v'}, \tag{13}$$

$$\overline{\sigma}\hat{\varpi} = \overline{\sigma \varpi} = \overline{\sigma}\,\overline{\varpi} + \overline{\sigma' \varpi'}, \tag{14}$$

where primes indicate deviations from the time mean. The residual thickness flux affects changes in the layer thickness through the thickness equation

$$\overline{\sigma}_{\tilde{t}} + (\overline{\sigma}\hat{u})_{\tilde{x}} + (\overline{\sigma}\hat{v})_{\tilde{y}} + (\overline{\sigma}\hat{\varpi})_{\tilde{b}} = 0, \tag{15}$$

where subscripts indicate partial differentiation. See Young (2012) for a more detailed introduction to the mathematical notation and derivation.

a. Meridional overturning circulation

In a statistically steady state, the zonal integral of (15) is

$$\int [(\overline{\sigma}\hat{v})_{\tilde{y}} + (\overline{\sigma}\hat{\varpi})_{\tilde{b}}\, d\tilde{x} = 0]. \tag{16}$$

This equation is identically satisfied when the integrated transports are written in terms of a residual-mean meridional overturning streamfunction $\psi^\sharp$ satisfying

$$\psi^\sharp_{\tilde{b}} \overset{\text{def}}{=} -\int \overline{\sigma}\hat{v}\, d\tilde{x}, \tag{17}$$

$$\psi^\sharp_{\tilde{y}} \overset{\text{def}}{=} \int \overline{\sigma}\hat{\varpi}\, d\tilde{x}. \tag{18}$$

Integrating (17) in buoyancy from the bottom (where $\tilde{b} = \psi^\sharp = 0$) gives

$$\psi^\sharp(\tilde{y}, \tilde{b}) = -\int\int_0^{\tilde{b}} \overline{\sigma}\hat{v}\, db'\, d\tilde{x}. \tag{19}$$

The analogous Eulerian-mean meridional overturning streamfunction is given by

$$\begin{aligned}\psi(\tilde{y}, \tilde{b}) &= \int\int_{-H}^{\tilde{\zeta}(\tilde{b})} \overline{v}^z\, dz\, d\tilde{x},\\ &= \int\int_0^{\tilde{b}} \overline{\sigma}\, \overline{v}^z\, db'\, d\tilde{x},\end{aligned} \tag{20}$$

where $\overline{v}^z$ is the meridional velocity averaged at constant depth and $\tilde{\zeta}(\tilde{b})$ is the average height of the isopycnal with buoyancy $\tilde{b}$. A method for accurately calculating $\overline{v}^z$ in buoyancy coordinates is given in appendix A. Contours of $\psi^\sharp$ which cross isopycnals indicate diapycnal flow. In contrast, contours of ψ which cross isopycnals indicate mean flow normal to mean isopycnals; in the limit of small slopes, this is approximately equivalent to the mean vertical velocity.

The eddy streamfunction $\psi^\star$ is obtained by subtracting the Eulerian-mean from the residual-mean streamfunction; that is,

$$\psi^\star = \psi^\sharp - \psi = -\int\int_0^{\tilde{b}} \overline{\sigma}(\hat{v} - \overline{v}^z)\, db'\, d\tilde{x}. \tag{21}$$

The eddy streamfunction is closely related to the zonally integrated meridional eddy flux of height. To see this, we derive an approximate expression for the Eulerian-mean velocity $\overline{v}^z$ using quantities defined in buoyancy coordinates. Let $b(z) = \tilde{b} + b'(z)$ be the instantaneous buoyancy at height z. Here $\tilde{b}$ is the mean buoyancy at z and we suppose that the buoyancy fluctuation b' is small. The Eulerian-mean velocity can then be written

$$\overline{v[b(z)]}^z = \overline{v(\tilde{b} + b')}^z \approx \overline{v(\tilde{b})} + \overline{b' v'_{\tilde{b}}}^z.$$

The first term on the RHS is the velocity averaged at constant buoyancy. The errors associated with evaluating the second term at $\tilde{b}$ and replacing the average at constant height with an average at constant buoyancy are second order and can be neglected if b' is sufficiently small; thus,

$$\overline{v}^z \approx \overline{v} + \overline{b' v'_{\tilde{b}}}. \tag{22}$$

Buoyancy fluctuations are related to height fluctuations by

$$b' \approx -\frac{\zeta'}{\overline{\sigma}},$$

so the Eulerian-mean velocity written in terms of buoyancy-coordinate quantities is

$$\overline{v}^z \approx \overline{v} - \frac{\overline{\zeta' v'_{\tilde{b}}}}{\overline{\sigma}}. \tag{23}$$

The difference between the residual and Eulerian mean velocities is

$$\hat{v} - \overline{v}^z \approx \frac{1}{\overline{\sigma}}(\overline{\zeta'_{\tilde{b}} v'} + \overline{\zeta' v'_{\tilde{b}}}) = \frac{1}{\overline{\sigma}}(\overline{\zeta' v'})_{\tilde{b}}, \tag{24}$$

and the eddy streamfunction is

$$\psi^\star(\tilde{y}, \tilde{b}) \approx -\int \overline{\zeta' v'}\, dx, \tag{25}$$

where we have used the fact that bottom is a material surface, so $\zeta' = 0$ there. Thus, the eddy streamfunction is approximately the negative of the net meridional eddy height flux. Note that unlike the analogous expressions for the eddy streamfunction in height coordinates derived from the transformed Eulerian mean (e.g., Plumb and Ferrari 2005) or the temporal residual mean (McDougall and McIntosh 2001), the eddy streamfunction defined in (25) naturally goes to zero at the surface and bottom instead of diverging there.

The residual MOC and its mean and eddy components in buoyancy coordinates are shown in Figs. 3a and 3b and 3c. The swash zone extends from the surface to the green line in Fig. 3. Substantial differences between $\psi^\sharp$ and ψ are found in the swash zone. Most of the downwelling in $\psi^\sharp$ is confined to the swash zone. This is a result of northward advection of buoyancy by the surface currents along the western and eastern boundaries and the subsequent loss of heat to the atmosphere. The cooled water sinks and is returned to the south nearly adiabatically where it upwells in the sponge layer. The eddies transport water northward in the swash zone and southward just below it. Weak counterclockwise cells are visible below $\tilde{b} = 0.01\ \mathrm{m\,s^{-2}}$ that are driven by diffusive upwelling in the interior and downwelling in the southern sponge.

The residual-mean meridional overturning streamfunction integrated in height coordinates,

$$\psi^{z,\sharp}(y, z) = -\int_{-H}^{z}\int \hat{v}\, dx\, dz', \tag{26}$$

offers a complementary perspective on the overturning circulation. The analogous Eulerian-mean streamfunction in height coordinates is given by

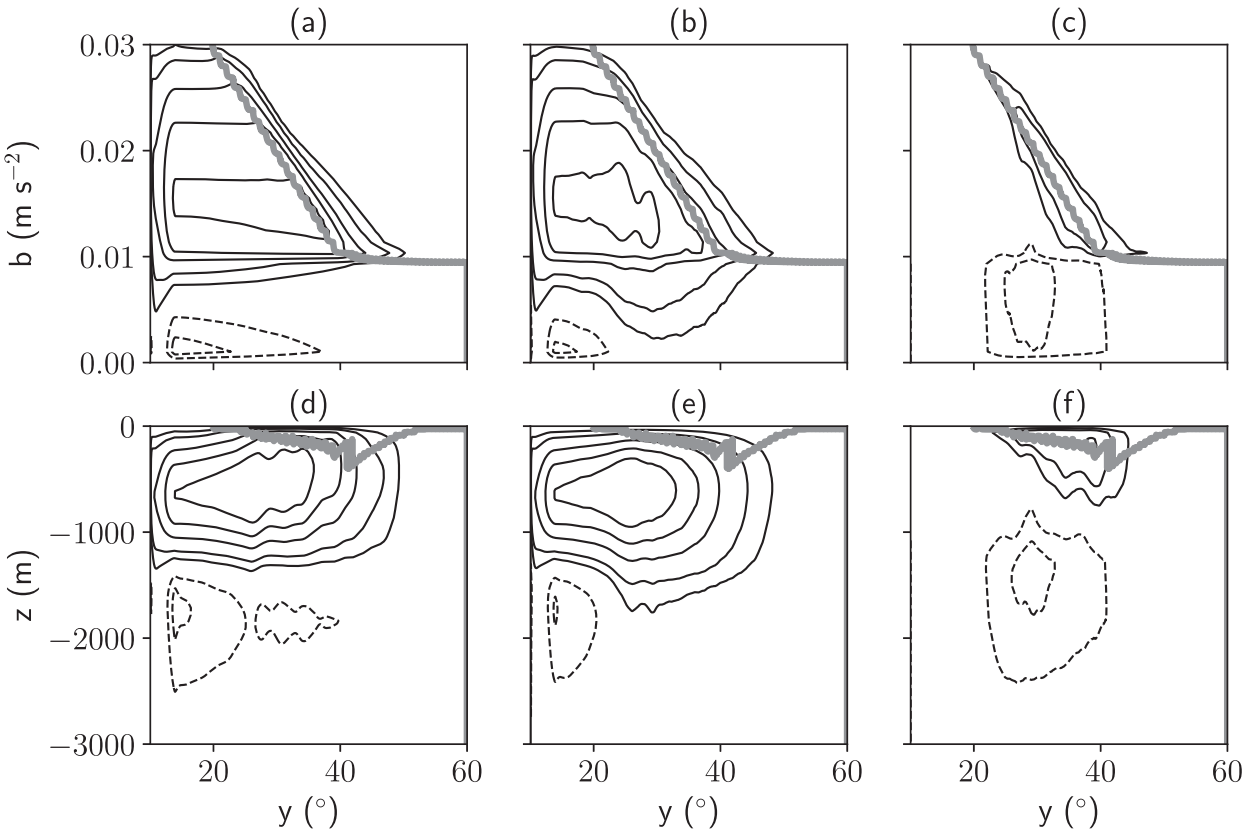

FIG. 3. (top) The (a) residual MOC $\psi^\sharp$, (b) its mean component ψ, and (c) its eddy component $\psi^\star$ (Sv) computed in buoyancy coordinates. (bottom) The (d) residual MOC $\psi^{z,\sharp}$, (e) its mean component ψ^z, and (f) its eddy component $\psi^\star$ (Sv) computed in height coordinates. The contours are drawn at ±2.5, ±5, ±10, ±15, and ±20 Sv; negative contours are dashed. The thick gray line indicates the bottom boundary of the swash zone.

$$\psi^z(y,z) = -\int_{-H}^{z}\int \overline{v}^z \, dx \, dz', \tag{27}$$

and the eddy streamfunction is $\psi^{z,\star} = \psi^{z,\sharp} - \psi^z$. Note that the zonal integration is along surfaces of constant buoyancy in (19) and (20) and at constant height in (26) and (27). Methods to calculate $\psi^{z,\sharp}$ and ψ^z accurately are given in appendix B. The decomposition of the residual-mean meridional overturning streamfunction into its Eulerian-mean and eddy components in height coordinates is shown in Figs. 3d–f. The residual-mean and Eulerian-mean flows show very similar patterns in height coordinates—upwelling in the sponge layer, followed by northward transport at surface, sinking at around 40°N, and southward transport near 1000 m. Eddies only play a significant role near the surface, where they transport water northward in the swash zone and southward just below it. The weak diffusive cells are found below about 1500 m.

Despite the similarity between the residual-mean and Eulerian-mean meridional flows, significant differences arise between the two in the zonal flows, which is explored in the next subsection. Specifically, the sinking takes place in a narrow eastern boundary layer in the Eulerian mean, flow while it is more spread out in the residual mean flow.

b. Zonal overturning circulation

The ZOC is derived in a manner analogous to the MOC, with the thickness equation integrated in the meridional rather than the zonal direction. The streamfunctions for the residual-mean and Eulerian-mean ZOC,

$$\chi^\sharp(\tilde{x},\tilde{b}) = -\int\int_0^{\tilde{b}} \overline{\sigma}\hat{u} \, db' \, d\tilde{y}, \tag{28}$$

and

$$\chi(\tilde{x},\tilde{b}) = -\int\int_0^{\tilde{b}} \overline{\sigma}\overline{u}^z \, db' \, d\tilde{y}, \tag{29}$$

respectively, can be defined as for the MOC. The eddy streamfunction is

$$\chi^\star(\tilde{x},\tilde{b}) = -\int\int_0^{\tilde{b}} \overline{\sigma}\,(\hat{u} - \overline{u}^z)\, db' \, d\tilde{y} \approx -\int\overline{\zeta' u'}\, d\tilde{y}. \tag{30}$$

The versions of the ZOC integrated at constant height are

$$\chi^{z,\sharp}(x,z) = -\int\int_{-H}^{z} \hat{u} \, dz' \, dy, \tag{31}$$

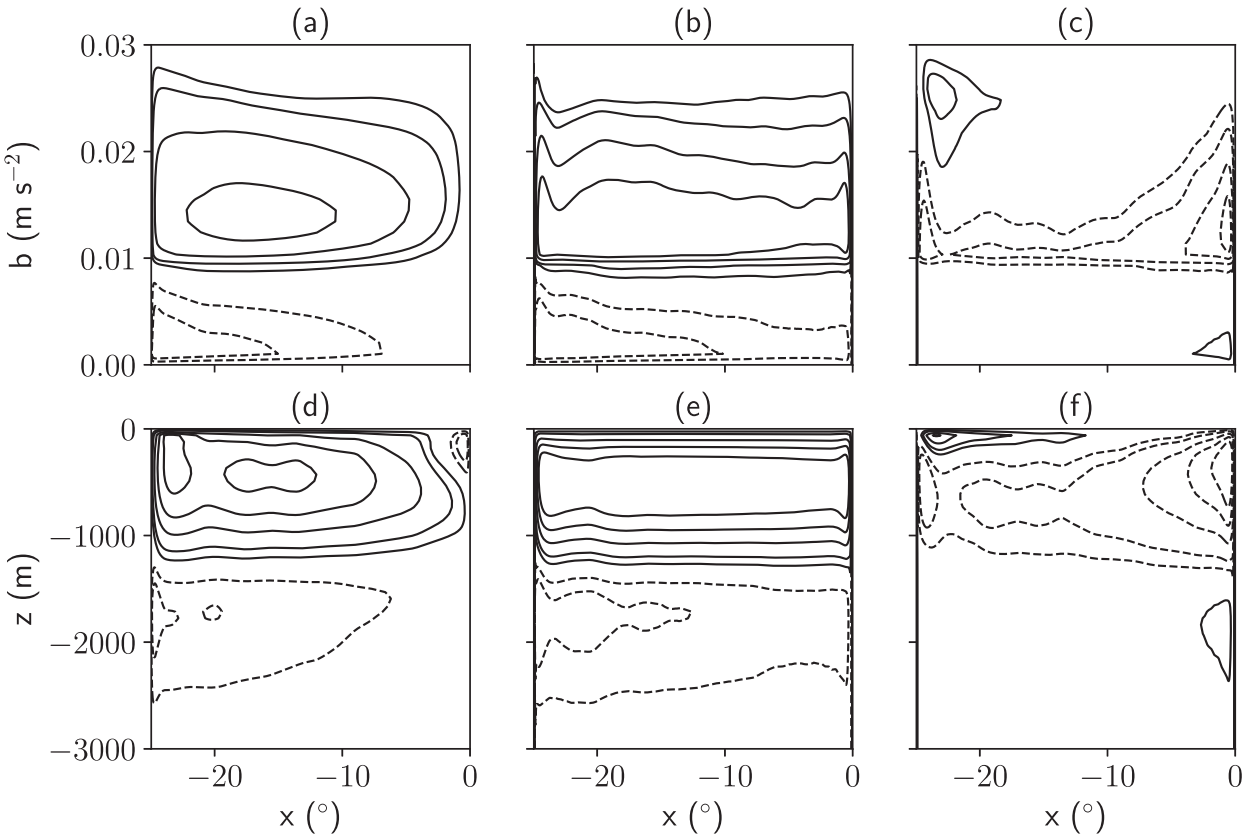

FIG. 4. As in Fig. 3, but for the ZOC.

and

$$\chi^z(x,z) = -\iint_{-H}^{z} \overline{u}^z \, dz' \, dy. \tag{32}$$

As with the MOC, the difference of the residual and mean streamfunctions gives the eddy streamfunctions $\chi^\star$ and $\chi^{z,\star}$.

The ZOC integrated along surfaces of constant buoyancy $\chi^\sharp$ and height $\chi^{z,\sharp}$ are shown in Figs. 4a and 4d, respectively. The upper circulation cell in Fig. 4a shows that there is diapycnal upwelling on the western boundary and broadly distributed diapycnal downwelling in the eastern two-thirds of the basin. In contrast, the Eulerian-mean vertical velocity is concentrated in very narrow boundary layers (Fig. 4b). The eddy component drives an opposing circulation that almost exactly cancels the Eulerian-mean flow on the eastern boundary (Fig. 4c).

The eastern broadening of the diapycnal downwelling boundary layer due to eddies is also evident in height coordinates (Fig. 4d), which also shows a small counterclockwise circulation near the surface on the eastern boundary. This cell is due to warm-core eddies shed by the eastern boundary which propagate westward into the interior and dissipate. This westward transport of buoyant water contributes to a westward residual velocity in the lightest buoyancy classes (cf. Bire and Wolfe 2018, Fig. 8). The near-surface residual eastern boundary circulation is therefore reversed compared to the mean (Fig. 4e). This reversed cell is not visible in the ZOC integrated along buoyancy surfaces $\chi^\sharp$ (Fig. 4a), since meridional integration along isopycnals includes contributions from the whole range of depths occupied by the isopycnals, obscuring the contribution from the surface. The appearance of the reversed near-surface cell in Fig. 4d emphasizes the subtleties involved with defining a 2D representation of the 3D overturning circulation. Such a reduction always involves a loss of information and, as such, no single coordinate system can be optimal in all situations.

Nevertheless, there is a consistent difference between the residual-mean and the Eulerian-mean streamfunctions in both the coordinate systems. In particular, the boundary layers in the Eulerian-mean streamfunctions are significantly narrower than those in the residual-mean streamfunctions.

The thermodynamics of diapycnal transformation can be further diagnosed by considering the separate contributions to the diapycnal velocity from the sponge layer, surface forcing, and interior diapycnal diffusion. The sponge layer contribution is diagnosed by meridionally integrating the diapycnal velocity over the meridional extent of the sponge layer. The surface forcing contribution is diagnosed by multiplying the diapycnal velocity at each isopycnal layer by 0 if the layer was not in the swash zone and then meridionally integrating over the region north of the sponge layer. Similarly, the contribution of the interior specified diapycnal diffusivity is diagnosed by

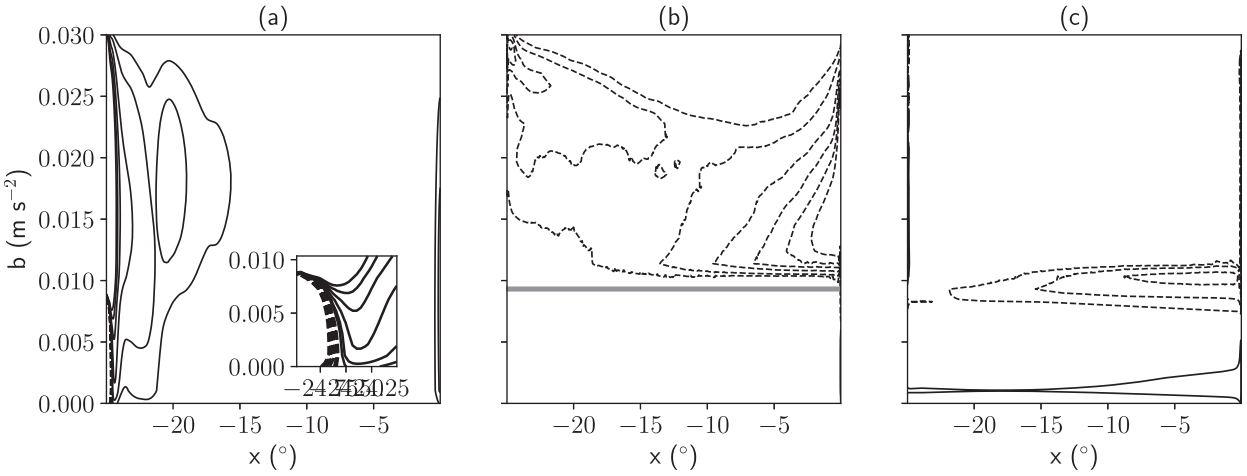

FIG. 5. The meridionally integrated diapycnal velocity (a) in the sponge layer (the inset shows the diapycnal velocity in the sponge layer very close to the western boundary), (b) due to surface forcing, and (c) due to interior diapycnal diffusion. The contours are drawn at ±2.5, ±5, ±10, ±15, ±20, and ±25 m^2 s^{-1}; negative contours are dashed. The thick gray line in (b) indicates the densest outcropping isopycnal.

multiplying the diapycnal velocity at each isopycnal layer by 0 if the layer was in the swash zone and then meridionally integrating over the region north of the swash zone. Formally, the components are

$$\chi^{\sharp}_{\tilde{x},\text{sponge}} \overset{\text{def}}{=} \int_{0}^{14^\circ\text{N}} \overline{\sigma\varpi}\, d\tilde{y}, \tag{33}$$

$$\chi^{\sharp}_{\tilde{x},\text{surface}} \overset{\text{def}}{=} \int_{14^\circ\text{N}}^{60^\circ\text{N}} \overline{\sigma\varpi}\mu\, d\tilde{y}, \tag{34}$$

$$\chi^{\sharp}_{\tilde{x},\text{interior}} \overset{\text{def}}{=} \int_{14^\circ\text{N}}^{60^\circ\text{N}} \overline{\sigma\varpi}(1-\mu)\, d\tilde{y}, \tag{35}$$

where $\mu = 1$ if the layer is in the swash zone and zero otherwise. A similar approach was applied by Xu et al. (2018) in a model with sigma coordinates, which behaved like height coordinates near the surface. They first calculated the area intersected at the surface by a narrow density band around a given density. They then integrated the density flux due to surface forcing over this area to calculate the total diapycnal flux across this density surface. One problem encountered by this approach is that it does not keep track of how long the isopycnal surface was at the surface. The flux is also only calculated at the surface, whereas their model allowed the surface heat flux to penetrate deeper. In the present study, the swash zone provides a very good estimate of how deep the surface cooling is felt. The only source of subjectivity is in the threshold defining the swash zone. We define the bottom of the swash zone as the densest isopycnal that outcrops at least 1% of the time (Fig. 2a), but the above decomposition is not sensitive to decreasing this threshold.

The three components of the diapycnal velocity are shown in Fig. 5. The diapycnal upwelling is concentrated in the sponge layer on the western boundary, while diapycnal downwelling is primarily due to surface forcing and occurs in a broad layer in the eastern half of the basin north of the sponge layer. The interior diffusivity component becomes active at deeper buoyancy levels near the interface between the surface layers and the abyssal; its contribution is small compared to the diapycnal transformation in the swash zone. The deep cell is driven by weak diffusive upwelling throughout the basin balanced by diapycnal downwelling in the sponge layer close to the western boundary [Figs. 5c and 5a (inset)].

5. Dynamics of the overturning circulations

In this section, we use the TWA momentum equations to determine to the physical processes driving the overturning circulations. The flux forms of the TWA momentum equations in buoyancy coordinates are

$$(\overline{\sigma}\hat{u})_{\tilde{t}} = -(\overline{\sigma}\hat{u}\hat{u})_{\tilde{x}} - (\overline{\sigma}\hat{u}\hat{v})_{\tilde{y}} - (\overline{\sigma}\hat{u}\hat{\varpi})_{\tilde{b}} - \overline{\sigma}\,\overline{m}_{\tilde{x}} + f\,\overline{\sigma}\hat{v} - \overline{\sigma}\nabla\cdot\mathbf{E}^{u}, \tag{36}$$

$$(\overline{\sigma}\hat{v})_{\tilde{t}} = -(\overline{\sigma}\hat{u}\hat{v})_{\tilde{x}} - (\overline{\sigma}\hat{v}\hat{v})_{\tilde{y}} - (\overline{\sigma}\hat{v}\hat{\varpi})_{\tilde{b}} - \overline{\sigma}\,\overline{m}_{\tilde{y}} - f\,\overline{\sigma}\hat{u} - \overline{\sigma}\nabla\cdot\mathbf{E}^{v}. \tag{37}$$

where

$$m = \frac{P}{\rho_0} + gz - \tilde{b}\zeta \tag{38}$$

is the Montgomery potential, which is analogous to pressure in buoyancy coordinates, and

$$\overline{\sigma}\nabla\cdot\mathbf{E}^{u} = (\overline{\sigma}\widehat{u''u''})_{\tilde{x}} + (\overline{\sigma}\widehat{u''v''})_{\tilde{y}} + (\overline{\sigma}\widehat{u''\varpi''})_{\tilde{b}} + \overline{\sigma' m'_{\tilde{x}}}, \tag{39}$$

$$\overline{\sigma}\nabla\cdot\mathbf{E}^{v} = (\overline{\sigma}\widehat{u''v''})_{\tilde{x}} + (\overline{\sigma}\widehat{v''v''})_{\tilde{y}} + (\overline{\sigma}\widehat{v''\varpi''})_{\tilde{b}} + \overline{\sigma' m'_{\tilde{y}}} \tag{40}$$

are the divergences of Eliassen–Palm flux vectors. See Young (2012) or Maddison and Marshall (2013) for proof that these terms can be written as a divergence. Double primes indicate deviations from TWA quantities. The first three terms in (39) and (40) represent divergences of Reynolds stresses while the

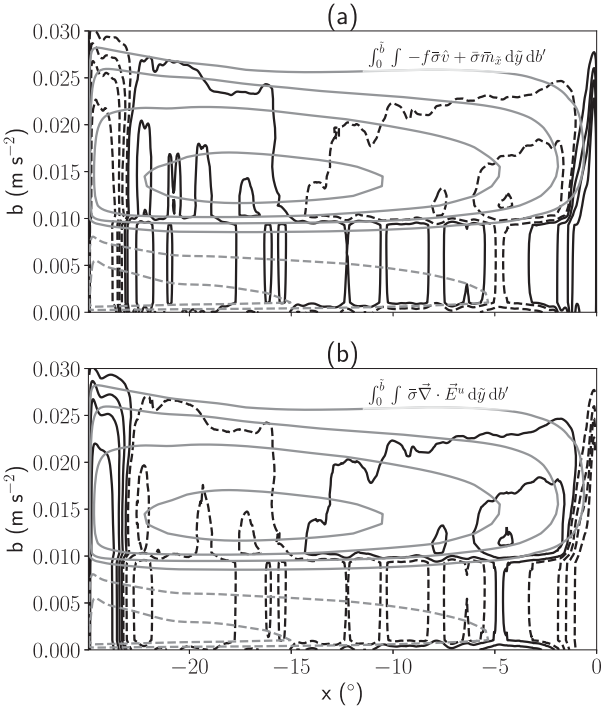

FIG. 6. The dominant terms contributing to the ZOC tendency [Eq. (41)] are (a) the ageostrophic Coriolis acceleration and (b) the divergence of the EP fluxes (both are shown in m^3 s^{-2} by black contours). The contours are drawn at -2×10^3, -1×10^3, -5×10^2, -1×10^2, 1×10^2, 5×10^2, 1×10^3, and 2×10^3. The gray contours represent the ZOC (Sv) and are drawn at −20, −15, −10, −5, −2, 2, 5, 10, 15, and 20. Negative contours are dashed.

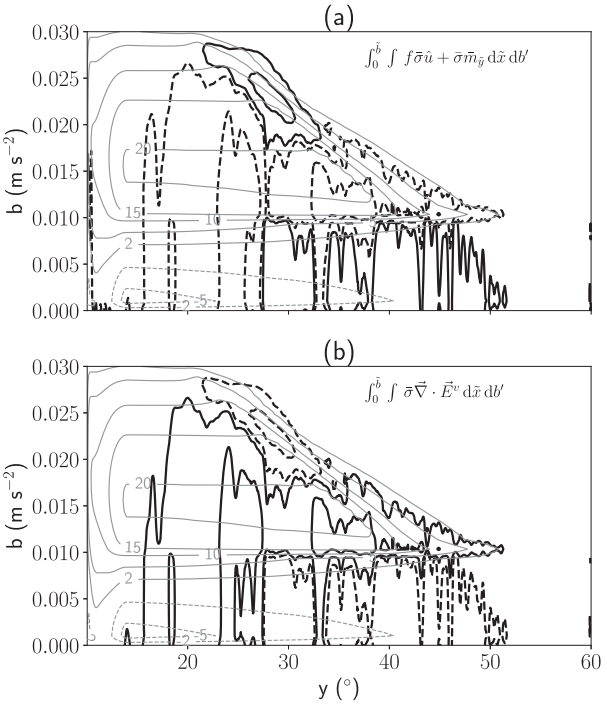

FIG. 7. The dominant terms contributing to the MOC tendency [Eq. (42)] are (a) the ageostrophic Coriolis acceleration and (b) the divergence of the EP fluxes (both are shown in m^3 s^{-2} by black contours). The contours are drawn at −500, −75, 75, and 500. The gray contours represent the ZOC (Sv) and are drawn at −20, −15, −10, −5, −2, 2, 5, 10, 15, and 20. Negative contours are dashed.

final term is called the form drag and homogenizes momentum in the vertical (e.g., Greatbatch 1998).

Meridionally and vertically integrating (36) and zonally and vertically integrating (37) gives the tendencies of zonal and meridional overturning streamfunctions, respectively, which are

$$\chi_t^\sharp = \int_0^{\bar{b}} \int [(\overline{\sigma}\hat{u}\hat{u})_{\tilde{x}} + (\overline{\sigma}\hat{u}\hat{\varpi})_{\tilde{b}} + \overline{\sigma}\overline{m}_{\tilde{x}} - f\overline{\sigma}\hat{v} + \overline{\sigma}\nabla \cdot \mathbf{E}^u]\, d\tilde{y}\, db', \tag{41}$$

$$\psi_t^\sharp = \int_0^{\bar{b}} \int [(\overline{\sigma}\hat{v}\hat{v})_{\tilde{y}} + (\overline{\sigma}\hat{v}\hat{\varpi})_{\tilde{b}} + \overline{\sigma}\overline{m}_{\tilde{y}} + f\overline{\sigma}\hat{u} + \overline{\sigma}\nabla \cdot \mathbf{E}^v]\, d\tilde{x}\, db'. \tag{42}$$

The dominant balance in the ZOC is geostrophy (not shown). To see the role of eddy fluxes in ZOC, we consider the next order balance which is between the ageostrophic Coriolis acceleration (Fig. 6a) and the divergence of Eliassen–Palm flux (Fig. 6b). The ageostrophic Coriolis acceleration tends to push the maximum of the upper cell westward while narrowing (broadening) the region of diapycnal transformation on the eastern (western) boundary. These tendencies are opposed by the divergence of the Eliassen–Palm flux. Physically, the ageostrophic circulation tends to oppose the residual overturning in the eastern half of the basin, but the constant supply of eddies from the eastern boundary, visible as positive tendency of the EP flux divergence, extends the diapycnal downwelling branch through the eastern half of the basin. Considering the individual components of the Eliassen–Palm fluxes, Reynolds stresses predominantly oppose the ageostrophic pressure gradient at the boundaries (not shown), while form drag opposes it in the interior as well as on the western boundary and weakly on the eastern boundary (not shown).

The MOC tendency is primarily a balance between the ageostrophic pressure gradient and the divergence of the EP fluxes (dominated by form drag). The ageostrophic pressure gradient tends to decelerate the upper circulation cell (Fig. 7a), which is countered by form drag (Fig. 7b). The Reynolds stress divergence is an order of magnitude smaller than these two terms. The reason why Reynolds stresses are significant in the ZOC but not in the MOC is that strong currents are found on the western and eastern boundaries but not on the southern and northern boundaries. Most of the zonal flow occurs in the interior of the domain instead of along the northern and southern boundaries. The Reynolds stress acts to slow the meridional boundary currents by decreasing the zonal pressure gradients; it therefore appears as a dissipative term in the ZOC tendency budget.

6. Parameterization of eddy transport

To better understand the role of eddies in the overturning circulations, it is useful to represent the eddy transport in terms

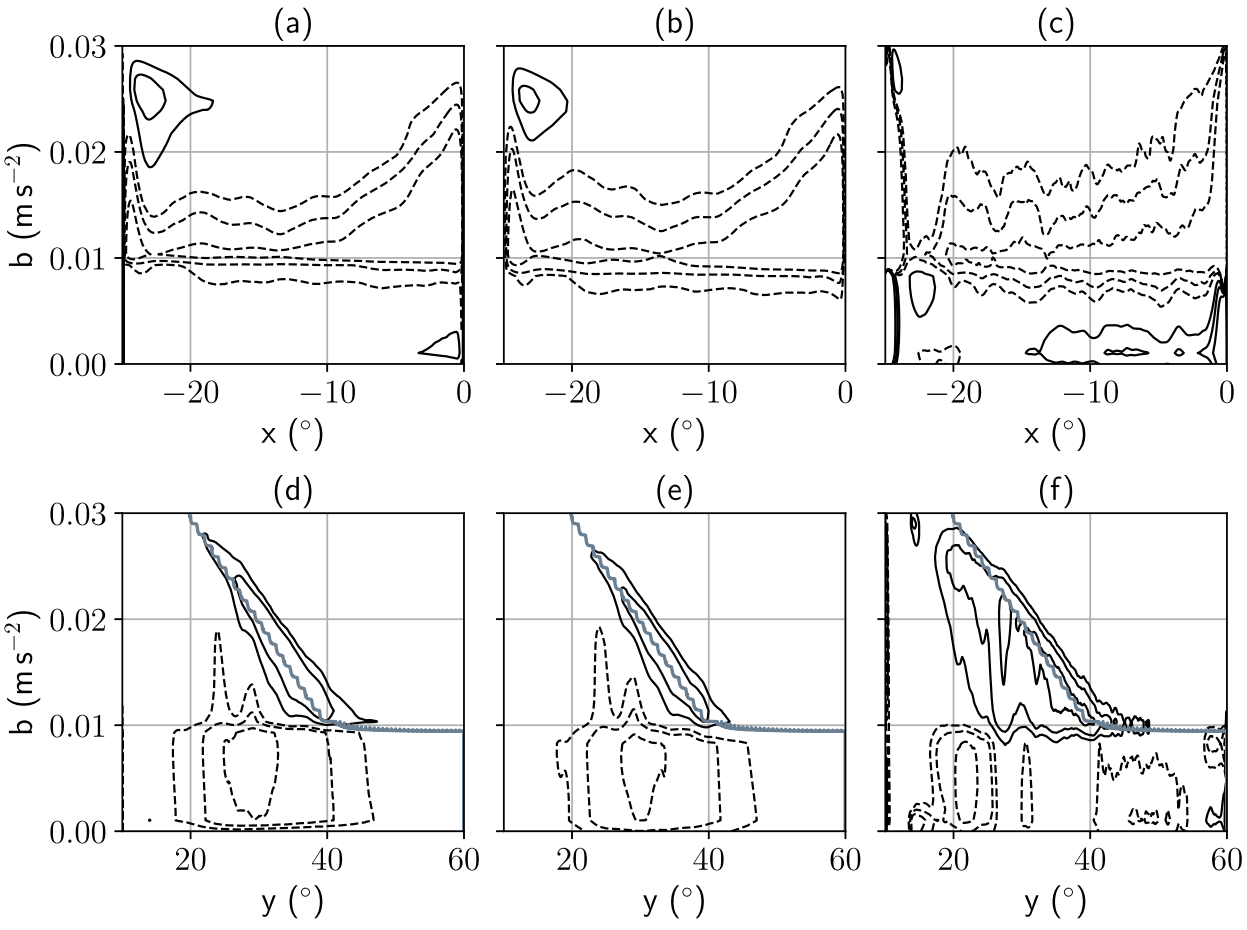

FIG. 8. (a) Eddy zonal overturning streamfunction $\chi^{\star}$, (b) meridionally integrated zonal eddy height flux, (c) RHS of (43) with K_x = 10 000 m^2 s^{-1}, (d) eddy meridional overturning streamfunction $\psi^{\star}$, (e) zonally integrated meridional eddy height flux, and (f) RHS of (44) with K_y = 8000 m^2 s^{-1}. Contours are drawn at −5, −2.5, −1, 2.5, 5, and 10 Sv. The eddy coefficients were obtained using least squares fits shown in Fig. 9. The gray line indicates the bottom boundary of the swash zone in (d)–(f).

of mean quantities on a basin scale. Following the discussion in section 4a, we express the eddy overturning streamfunction as the integrated eddy height flux. We then invoke flux–gradient relationship to write

$$\chi^* \approx -\int \overline{\zeta' u'}\, d\tilde{y} \approx K_x \int \overline{\zeta}_{\tilde{x}}\, d\tilde{y}, \tag{43}$$

$$\psi^* \approx -\int \overline{\zeta' v'}\, d\tilde{x} \approx K_y \int \overline{\zeta}_{\tilde{y}}\, d\tilde{x}, \tag{44}$$

where K_x and K_y are diffusivities. The eddy streamfunctions (left column of Fig. 8) are well approximated by the integrated eddy height fluxes (center column of Fig. 8); the visual similarity was confirmed through scatterplots, where the points were scattered around a line with slope 1 (not shown). The similarity between the eddy height fluxes and the mean height gradients (center and right columns of Fig. 8) in the interior suggests that the flux–gradient parameterization is a reasonable approximation.

The zonal eddy height diffusivities for the upper and lower cells of the ZOC are 10 000 m^2 s^{-1} and 3600 m^2 s^{-1}, respectively, as given by the slopes of the solid black and dashed gray lines in Fig. 9a. A region of width 2.5° from the western and eastern boundaries was ignored for calculating these diffusivities because near the boundaries the eddy-induced streamfunction becomes small but the gradient of interface heights increases. Bire and Wolfe (2018) attributed this to the suppression of eddy mixing by the presence of strong mean currents (Ferrari and Nikurashin 2010) and the boundary. The eddy component of the upper, clockwise MOC cell (Fig. 8d) is reasonably well represented by the mean height gradient (Fig. 8f), although the flux–gradient parameterization does a poor job representing the eddy component of the deep, counterclockwise MOC cell (not shown). In Fig. 9b, the fit between eddy meridional overturning and mean meridional height gradient is shown only for points lying in the swash zone. The fit deteriorates significantly if we include points outside the swash zone as the effect of eddies is not felt in the deeper layers especially in the southern part of the domain. The meridional coefficient of height diffusivity obtained from least squares fit (gray line in Fig. 9b) is 8000 m^2 s^{-1}.

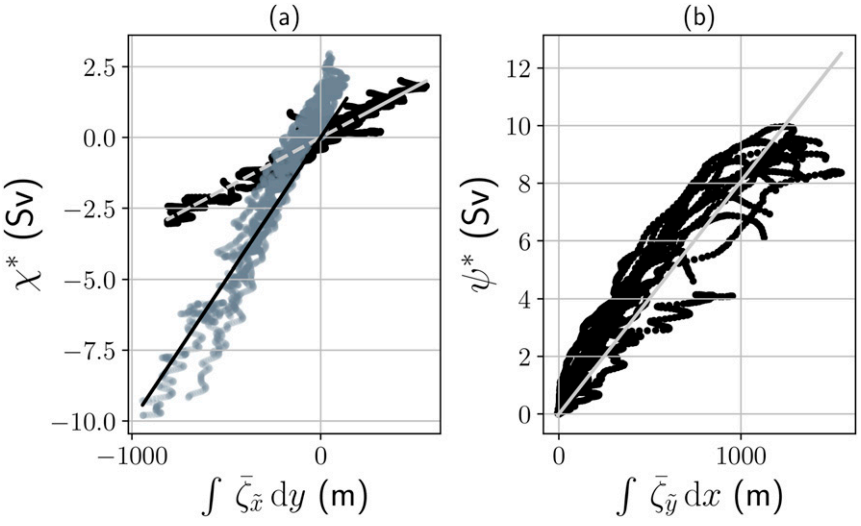

FIG. 9. (a) RHS of (43) vs $\chi^\star$ (black and gray markers indicate lower and upper overturning cells, respectively) and the least squares fit (gray and black lines). Gray and black lines are for the lower and upper overturning cells, respectively. (b) RHS of (44) vs $\psi^\star$ (black markers) and the least squares fit (gray line).

7. Scaling theory for the overturning transport

A scaling theory for the overturning circulations can be obtained from a volume budget in the spirit of Gnanadesikan (1999). The argument proceeds by considering transport across a pycnocline of depth h which outcrops a distance L_y from the southern boundary. The buoyancy difference across the pycnocline is Δb, which is set by the imposed surface temperature difference defined in (5). We focus on the MOC first; the scaling for the ZOC is identical. A schematic of the volume budget is shown in Fig. 10.

The processes which transport fluid across the pycnocline are diffusive upwelling T_d, geostrophic overturning driven by water sinking in the northern part of the forcing region T_n, and upwelling or downwelling in the southern sponge layer T_s. The scales for diffusive upwelling and northern overturning are

$$T_d \sim \frac{\kappa L_x L_y}{h} \quad \text{and} \quad T_n \sim \frac{\Delta b h^2}{f_N}, \tag{45}$$

respectively, where κ is the diapycnal diffusivity, L_x is the zonal extent of the basin, and f_N is the Coriolis parameter at the pycnocline outcrop latitude. The diffusive scaling arises from the one-dimensional advective–diffusive balance envisioned by Munk (1966). The scale for northern overturning is derived by considering thermal wind balance applied to the outcropping pycnocline and has been used extensively in scaling theories of the overturning circulation (e.g., Spall and Pickart 2001; Cessi and Wolfe 2009; Nikurashin and Vallis 2012; Jones and Cessi 2016; Jansen and Nadeau 2016; Ferrari et al. 2017a). The sponge layer relaxes isopycnal heights to a specified profile over a time $t_\star$, so the scale for the transport in the sponge layer is

$$T_s = \frac{h - h_\star}{t_\star} L_x L_s, \tag{46}$$

where $h_\star$ is the pycnocline target depth. Since the southern relaxation target has uniform buoyancy frequency, N, in the upper 1500 m, $h_\star = \Delta b / N^2$. Note that T_{bot} is less than the minimum surface temperature, so $h_\star < D_{\text{abyss}}$. The transports due to the three components sum to zero, which gives

$$\frac{h - h_\star}{t_\star} L_x L_s + \frac{\kappa}{h} L_x L_y = \frac{\Delta b h^2}{f_N}. \tag{47}$$

The relaxation time scale $t_\star$ is very short, so the dominant balance in (47) is

$$\frac{h - h_\star}{t_\star} L_x L_s = \frac{\Delta b h^2}{f_N}, \tag{48}$$

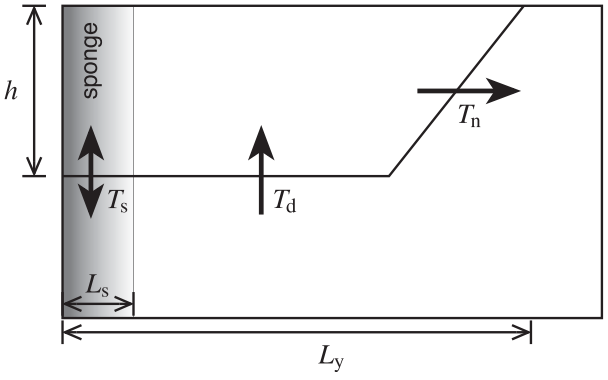

FIG. 10. Schematic of the MOC for the pycnocline volume budget. Diffusive transport T_d adds volume to the pycnocline that is removed by northern overturning T_n. Transport in the sponge T_s can be of either sign depending on the parameter regime. The pycnocline has depth h and meridional extent L_y; L_s is the width of the sponge layer.

which gives

$$h = h_0 \overset{\text{def}}{=} h_\star \frac{1-\sqrt{1-4\tau}}{2\tau} \approx h_\star(1+\tau), \tag{49}$$

where

$$\tau \overset{\text{def}}{=} \frac{\Delta b^2}{f_N N^2 L_x L_s} t_\star \tag{50}$$

is a nondimensional measure of the relaxation time scale. For the "control" parameters, $\tau \approx 0.07$, so $h \approx h_\star$. The strength of the northern overturning in this limit is

$$T_n \sim \frac{\Delta b h_\star^2}{f_N} = \frac{\Delta b^3}{f_N N^4} \sim 20\,\text{Sv}, \tag{51}$$

while the diffusive upwelling is only

$$T_d \sim \frac{\kappa}{h_\star} L_x L_y \sim 1\,\text{Sv}. \tag{52}$$

Although the vertical diffusivity κ is large compared to observed values in the upper ocean, diffusive overturning is weak because the basin is narrow and the pycnocline relatively deep. Note that since the basin width L_x appears in the denominator of τ, increasing L_x would lead to a slight reduction in both the pycnocline depth and the overturning strength.

The lowest-order diffusive correction to the pycnocline depth is

$$\Delta h = -\epsilon \frac{h_\star}{2 - \dfrac{h_0}{h_\star}} \approx -\epsilon h_\star, \tag{53}$$

where

$$\epsilon \overset{\text{def}}{=} \frac{\kappa t_\star}{h_\star^2} \frac{L_y}{L_s} = \frac{\kappa t_\star N^4}{\Delta b^2} \frac{L_y}{L_s} \tag{54}$$

is a measure of the relative strength of the diffusively driven circulation to the relaxation-driven circulation. For the control parameters, $\epsilon \approx 3 \times 10^{-4}$. Since the correction to h is negative, the lowest-order effect of diffusion is to make the pycnocline shallower. The diffusive correction to northern overturning is

$$\Delta T_n \approx \frac{2\Delta b h_0}{f_N} \Delta h \approx -2\epsilon T_n, \tag{55}$$

to lowest order. This correction is small and *negative*—the diffusive overturning has the opposite sense as the upper-ocean overturning, so increasing the diapycnal diffusivity would *decrease* the strength of the overturning. This is in contrast to previous studies that show that the overturning scales as $\kappa^{2/3}$ (e.g., Bryan 1987; de Verdière 1988; Park and Bryan 2000). In the aforementioned studies, the diffusively upwelled water is balanced by sinking in the Northern Hemisphere as summarized by Gnanadesikan (1999). Our paradoxical dependence of the overturning on diffusivity is due to the fact that diffusively upwelled water is balanced by downwelling in the sponge layer rather than in the northern sinking region, resulting in a diffusive circulation that cancels rather than enhances the main overturning cell.

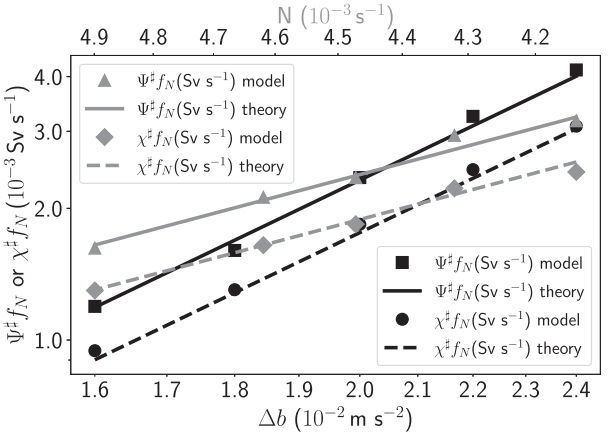

FIG. 11. Scaling of the MOC (black squares) and ZOC (black circles) with the imposed surface buoyancy change Δb. The black lines follow Δb^3. Scaling of the MOC (gray triangles) and ZOC (gray diamonds) with the imposed southern boundary buoyancy frequency. The gray lines follow N^4.

In our physical setting, the northern overturning scaling (51) shows that the MOC is directly proportional to the cube of the meridional buoyancy gradient imposed at the surface and inversely proportional to the fourth power of the stratification imposed at the southern boundary of the domain. This is because the depth of the pycnocline is set by the stratification imposed at the southern boundary. In a more realistic simulation which includes the Southern Ocean, the depth scale would be set by a balance between Southern Ocean overturning, diapycnal diffusion, and northern sinking (e.g., Gnanadesikan 1999; Wolfe and Cessi 2010; Nikurashin and Vallis 2012).

Additionally, the majority of the meridional transport is carried in the western (south of 30°N) and eastern (north of 30°N) boundary currents which are, in turn, fed by the baroclinic zonal flow connecting the two boundaries. We thus expect the ZOC and the boundary current transports to follow the same scaling as the MOC. This close connection between the MOC and ZOC was also invoked by Nikurashin and Vallis (2012) as a motivation for their northern overturning scaling.

The maximum of the zonal and meridional streamfunctions are plotted against change in surface buoyancy and stratification at the southern boundary in Fig. 11. The agreement with the scaling (51) is excellent. The scaling also collapses the transports of the surface eastern boundary currents from different experiments into a single curve (Fig. 12). This verifies the assertion that most of the MOC transport takes place in the boundary currents.

As expected, reducing the diapycnal diffusivity leads to small but systematic increases in the overturning strength (not shown).

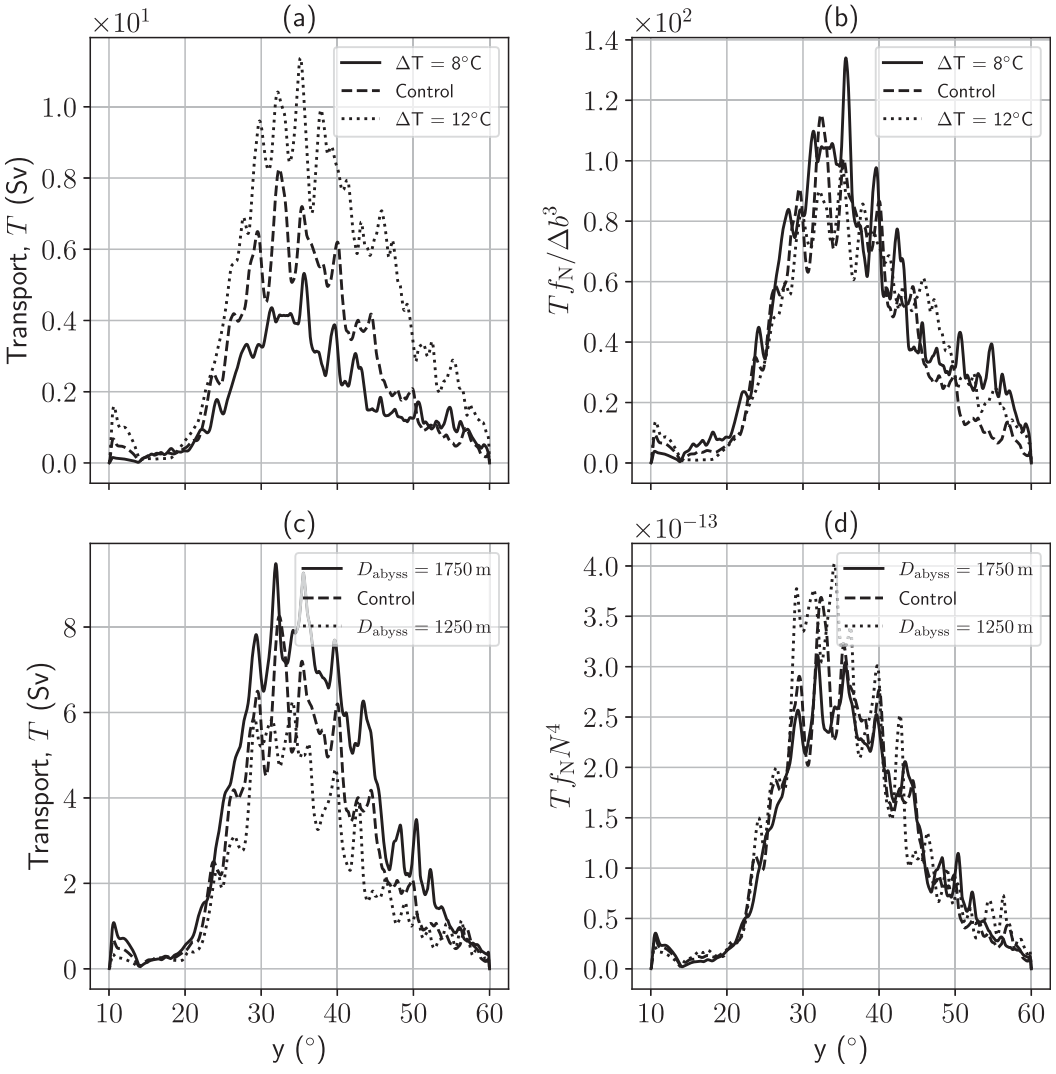

FIG. 12. (a) Meridional transport by the northward eastern boundary current (Sv) as a function of latitude for three cases with varying surface forcing. (b) As in (a), but scaled by Δb^{-3}. (c) As in (a), but for three cases with varying stratification at the southern boundary. (d) As in (c), but scaled by N^4.

8. Summary and discussion

This study emphasizes the distinction between vertical motion and diapycnal transformation. Care should be taken to avoid conflating the two processes in discussions of upwelling and downwelling. For the main overturning cell, most diapycnal upwelling is confined to the sponge layer in the southern part of the domain, with diapycnal downwelling due to surface forcing as well as interior diffusion. The abyssal overturning cell is characterized by interior upwelling and downwelling in the sponge layer. The distinction between the locations of vertical downwelling and diapycnal downwelling is stark. The vertical downwelling is mostly adiabatic and results from vertical excursions of isopycnals due to eddies and eastward zonal flow along downward sloping isopycnals. Most vertical downwelling is confined to the thin ''hydrostatic layers'' near the boundaries. On the other hand, diapycnal transformation occurs over a broad region extending westward from the eastern boundary. This broadening is achieved by the action of eddies carrying warm water from the eastern boundary into the interior where their thermal anomalies are eroded by the surface forcing. The western boundary layer also broadens to the east but this is not as pronounced as on the eastern boundary, likely because of the tendency of disturbances to propagate westward.

Examination of the overturning tendencies derived from the momentum equations shows that eddies tend to oppose the large-scale overturning through the action of the form drag and Reynolds stress divergence. The eddy-driven overturning can be represented as a horizontally integrated flux of eddy interface height, which can be further parameterized as a constant times the gradient of mean interface height.

A scaling for the overturning circulation based on a balance between geostrophic overturning and upwelling in the sponge

layer is derived and compared to the numerical simulations. Both the zonal and meridional overturning circulations vary with the cube of the surface buoyancy gradient and inversely with the fourth power of the stratification at the southern boundary. The transport by the eastern boundary current follows the same scaling, an indication that most of the meridional overturning circulation takes place in the boundary currents. Unlike previous studies, which show that the overturning transport scales as $\kappa^{2/3}$ (e.g., Bryan 1987; de Verdière 1988; Park and Bryan 2000), the diapycnal diffusivity is not significant in setting the scales of transport in our study. Our model is essentially a specialized case of the second solution proposed by Gnanadesikan (1999) where the thermocline depth and overturning transport both appear as functions of diffusivity, viscosity, Southern Ocean wind, and buoyancy forcing. In our model the effect of the Southern Ocean is approximated by a sponge layer where the thermocline depth is prescribed and overturning strength is diagnosed.

Many features of the idealized setup discussed here are unrealistic to varying degrees. Perhaps the greatest departure from the physics of the World Ocean is the southern sponge layer, which provides an external control on the background stratification. If the basin were extended to include the Southern Ocean, the diapycnal upwelling that closes the MOC would occur in two stages—first as vertical upwelling along sloping isopycnals and then as diapycnal northward flow in the surface mixed layer (e.g., Wolfe and Cessi 2010; Nikurashin and Vallis 2011). If there were more than a single basin, some of the diapycnal transformation would also occur in other basins (e.g., Marshall and Speer 2012; Talley 2013; Jones and Cessi 2016; Ferrari et al. 2017a). The sponge layer is intended to achieve the net effect of all of these processes, at least qualitatively.

Nevertheless, the study convincingly demonstrates the difference between vertical motion and diapycnal transformation in the boundary currents. While vertical motions are confined to very narrow boundary layers, these arise mostly from the vertical movement of the isopycnals and flow along sloping isopycnals. Diapycnal transformation takes place in the very broad boundary layers whose width is determined by the distance an eddy can travel before being damped by surface forcing and internal diffusion. This result is noteworthy because it sheds light on the possible fundamental mechanisms in driving the downwelling branch of the Atlantic meridional overturning circulation. The warm water originating from the North Atlantic Drift enters the Labrador, Greenland, and Nordic Seas and exits at deeper levels as cold boundary currents (e.g., Childers et al. 2015; Rossby et al. 2018). Consistent with previous studies (e.g., Spall 2004, 2010, 2011; Katsman et al. 2018; Xu et al. 2018; Brüggemann and Katsman 2019), our study shows that the densification of water happens over a broad area rather than in narrow boundary layers. Although the deep-water formation sites in the North Atlantic are known to be broadly located in the Labrador Sea and the Greenland Sea, how much of the diapycnal transformation takes place in the boundary currents and in the open ocean is still an open question. The current study, in an idealized eddy-resolving setup, shows that the diapycnal transformation first happens in the surface warm eastern boundary current as it crosses outcropping isopycnals and then in the warm eddies in the interior.

Acknowledgments. This research was funded by NSF Grant OC-1559065. This work used the Extreme Science and Engineering Discovery Environment (XSEDE) Stampede cluster at the Texas Advanced Computing Center through the allocation TG-OCE160008. The authors are thankful to the helpful and responsive team at NOAA-GFDL involved in developing MOM6 as well as to the Python community for providing free and open source tools like Jupyter, Numpy, SciPy, Matplotlib, and Xarray. The authors would also like to thank Dong-Ping Wang, Robert Hallberg, Michael Spall, and an anonymous reviewer for several helpful comments and suggestions.

APPENDIX A

Calculation of Eulerian-Mean Velocities in Buoyancy Coordinates

Since the model output is in isopycnal coordinates, care must be taken to ensure that Eulerian-mean velocity in isopycnal coordinates is calculated accurately. To conserve transport while interpolating from isopycnal coordinates to height coordinates, the vertically integrated transport,

$$\mathbf{T} = \int_{-H}^{\bar{b}} \sigma \mathbf{u}\, db', \tag{A1}$$

where $\mathbf{u}$ is the horizontal velocity, is first calculated. This quantity is then linearly interpolated to the mean heights of the isopycnals. The meridional velocity at the heights of the isopycnal layers is then given by

$$\mathbf{u}(z,t) = \frac{\partial \mathbf{T}}{\partial z}. \tag{A2}$$

This process is repeated for each time step. Taking a time mean of $\mathbf{u}$ in (A2) gives the Eulerian-mean velocity in isopycnal coordinates.

APPENDIX B

Overturning Streamfunctions Integrated in Height Coordinates

Here we describe the method used to obtain the meridional overturning streamfunction integrated in height coordinates. The analogous zonal overturning streamfunction is obtained in the same manner.

The residual-mean streamfunction integrated in height coordinates is

$$\begin{aligned}\psi^{z,\sharp}(y,z) &= -\int\int_{-H}^{z} \hat{v}\, dz'\, dx,\\ &= \int\int_{0}^{b^{\sharp}(z)} \overline{\sigma v}\, db'\, dx.\end{aligned} \tag{B1}$$

Here, $b^{\sharp}$ is the effective buoyancy field, which satisfies

$$b^\sharp[\overline{\zeta}(\tilde{b})] = \tilde{b}.$$

The first of (B1) requires $\hat{v}$ to be interpolated into height coordinates, which becomes inaccurate near the surface and bottom where $\overline{\sigma}^{-1} \to \infty$. We instead use the second of (B1), which states that the vertical integration is carried out in isopycnal coordinates and the result interpolated into height coordinates. The meridional integration is then performed at constant height to obtain an accurate estimate of $\psi^{z,\sharp}$. The Eulerian-mean streamfunction is

$$\psi^z(y,z) = -\int\int_{-H}^{z} \overline{v}^z \, dz' \, dx, \tag{B2}$$

where $\overline{v}^z$ is obtained using the method described in appendix A.

REFERENCES

Allison, L. C., H. L. Johnson, and D. P. Marshall, 2011: Spin-up and adjustment of the Antarctic Circumpolar current and global pycnocline. *J. Mar. Res.*, **69**, 167–189, https://doi.org/10.1357/002224011798765330.

Andrews, D. G., and M. E. McIntyre, 1976: Planetary waves in horizontal and vertical shear: The generalized Eliassen–Palm relation and the mean zonal acceleration. *J. Atmos. Sci.*, **33**, 2031–2048, https://doi.org/10.1175/1520-0469(1976)033<2031:PWIHAV>2.0.CO;2.

Barcilon, V., and J. Pedlosky, 1967: A unified linear theory of homogeneous and stratified rotating fluids. *J. Fluid Mech.*, **29**, 609–621, https://doi.org/10.1017/S0022112067001053.

Bire, S., and C. L. P. Wolfe, 2018: The role of eddies in buoyancy-driven eastern boundary currents. *J. Phys. Oceanogr.*, **48**, 2829–2850, https://doi.org/10.1175/JPO-D-18-0040.1.

Brüggemann, N., and C. A. Katsman, 2019: Dynamics of downwelling in an eddying marginal sea: Contrasting the Eulerian and the isopycnal perspective. *J. Phys. Oceanogr.*, **49**, 3017–3035, https://doi.org/10.1175/JPO-D-19-0090.1.

Bryan, F., 1987: Parameter sensitivity of primitive equation ocean general circulation models. *J. Phys. Oceanogr.*, **17**, 970–985, https://doi.org/10.1175/1520-0485(1987)017<0970:PSOPEO>2.0.CO;2.

Cessi, P., and C. L. Wolfe, 2009: Eddy-driven buoyancy gradients on eastern boundaries and their role in the thermocline. *J. Phys. Oceanogr.*, **39**, 1595–1614, https://doi.org/10.1175/2009JPO4063.1.

——, and ——, 2013: Adiabatic eastern boundary currents. *J. Phys. Oceanogr.*, **43**, 1127–1149, https://doi.org/10.1175/JPO-D-12-0211.1.

——, and C. S. Jones, 2017: Warm-route versus cold-route interbasin exchange in the meridional overturning circulation. *J. Phys. Oceanogr.*, **47**, 1981–1997, https://doi.org/10.1175/JPO-D-16-0249.1.

——, C. L. Wolfe, and B. C. Ludka, 2010: Eastern-boundary contribution to the residual and meridional overturning circulations. *J. Phys. Oceanogr.*, **40**, 2075–2090, https://doi.org/10.1175/2010JPO4426.1.

Childers, K. H., C. N. Flagg, T. Rossby, and C. Schrum, 2015: Directly measured currents and estimated transport pathways of Atlantic water between 59.5°N and the Iceland–Faroes–Scotland Ridge. *Tellus*, **67A**, 28067, https://doi.org/10.3402/tellusa.v67.28067.

De Szoeke, R. A., and A. F. Bennett, 1993: Microstructure fluxes across density surfaces. *J. Phys. Oceanogr.*, **23**, 2254–2264, https://doi.org/10.1175/1520-0485(1993)023<2254:MFADS>2.0.CO;2.

de Verdière, C. A., 1988: Buoyancy driven planetary flows. *J. Mar. Res.*, **46**, 215–265, https://doi.org/10.1357/002224088785113667.

Ferrari, R., and M. Nikurashin, 2010: Suppression of eddy diffusivity across jets in the Southern Ocean. *J. Phys. Oceanogr.*, **40**, 1501–1519, https://doi.org/10.1175/2010JPO4278.1.

——, L.-P. Nadeau, D. P. Marshall, L. C. Allison, and H. L. Johnson, 2017a: A model of the ocean overturning circulation with two closed basins and a reentrant channel. *J. Phys. Oceanogr.*, **47**, 2887–2906, https://doi.org/10.1175/JPO-D-16-0223.1.

——, ——, ——, ——, and ——, 2017b: A model of the ocean overturning circulation with two closed basins and a reentrant channel. *J. Phys. Oceanogr.*, **47**, 2887–2906, https://doi.org/10.1175/JPO-D-16-0223.1.

Georgiou, S., C. G. van der Boog, N. Brüggemann, S. L. Ypma, J. D. Pietrzak, and C. A. Katsman, 2019: On the interplay between downwelling, deep convection and mesoscale eddies in the Labrador Sea. *Ocean Modell.*, **135**, 56–70, https://doi.org/10.1016/j.ocemod.2019.02.004.

Gnanadesikan, A., 1999: A simple predictive model for the structure of the oceanic pycnocline. *Science*, **283**, 2077–2079, https://doi.org/10.1126/science.283.5410.2077.

Greatbatch, R. J., 1998: Exploring the relationship between eddy-induced transport velocity, vertical momentum transfer, and the isopycnal flux of potential vorticity. *J. Phys. Oceanogr.*, **28**, 422–432, https://doi.org/10.1175/1520-0485(1998)028<0422:ETRBEI>2.0.CO;2.

Griffies, S. M., and R. W. Hallberg, 2000: Biharmonic friction with a Smagorinsky-like viscosity for use in large-scale eddy-permitting ocean models. *Mon. Wea. Rev.*, **128**, 2935–2946, https://doi.org/10.1175/1520-0493(2000)128<2935:BFWASL>2.0.CO;2.

Haney, R. L., 1971: Surface thermal boundary condition for ocean circulation models. *J. Phys. Oceanogr.*, **1**, 241–248, https://doi.org/10.1175/1520-0485(1971)001<0241:STBCFO>2.0.CO;2.

Jansen, M. F., and L.-P. Nadeau, 2016: The effect of Southern Ocean surface buoyancy loss on the deep-ocean circulation and stratification. *J. Phys. Oceanogr.*, **46**, 3455–3470, https://doi.org/10.1175/JPO-D-16-0084.1.

Jones, C. S., and P. Cessi, 2016: Interbasin transport of the meridional overturning circulation. *J. Phys. Oceanogr.*, **46**, 1157–1169, https://doi.org/10.1175/JPO-D-15-0197.1.

Katsman, C. A., S. S. Drijfhout, H. A. Dijkstra, and M. A. Spall, 2018: Sinking of dense North Atlantic waters in a global ocean model: Location and controls. *J. Geophys. Res. Oceans*, **123**, 3563–3576, https://doi.org/10.1029/2017JC013329.

Maddison, J. R., and D. P. Marshall, 2013: The Eliassen–Palm flux tensor. *J. Fluid Mech.*, **729**, 69–102, https://doi.org/10.1017/jfm.2013.259.

Marshall, J., and T. Radko, 2003: Residual-mean solutions for the Antarctic Circumpolar Current and its associated overturning circulation. *J. Phys. Oceanogr.*, **33**, 2341–2354, https://doi.org/10.1175/1520-0485(2003)033<2341:RSFTAC>2.0.CO;2.

——, and ——, 2006: A model of the upper branch of the meridional overturning of the southern ocean. *Prog. Oceanogr.*, **70**, 331–345, https://doi.org/10.1016/j.pocean.2006.07.004.

——, and K. Speer, 2012: Closure of the meridional overturning circulation through Southern Ocean upwelling. *Nat. Geosci.*, **5**, 171–180, https://doi.org/10.1038/ngeo1391.

Mazloff, M. R., R. Ferrari, and T. Schneider, 2013: The force balance of the Southern Ocean meridional overturning

circulation. *J. Phys. Oceanogr.*, **43**, 1193–1208, https://doi.org/10.1175/JPO-D-12-069.1.

McDougall, T. J., and P. C. McIntosh, 2001: The temporal-residual-mean velocity. Part II: Isopycnal interpretation and the tracer and momentum equations. *J. Phys. Oceanogr.*, **31**, 1222–1246, https://doi.org/10.1175/1520-0485(2001)031<1222:TTRMVP>2.0.CO;2.

Munk, W. H., 1966: Abyssal recipes. *Deep-Sea Res. Oceanogr. Abstr.*, **13**, 707–730, https://doi.org/10.1016/0011-7471(66)90602-4.

Nikurashin, M., and G. Vallis, 2011: A theory of deep stratification and overturning circulation in the ocean. *J. Phys. Oceanogr.*, **41**, 485–502, https://doi.org/10.1175/2010JPO4529.1.

——, and ——, 2012: A theory of the interhemispheric meridional overturning circulation and associated stratification. *J. Phys. Oceanogr.*, **42**, 1652–1667, https://doi.org/10.1175/JPO-D-11-0189.1.

Park, Y.-G., and K. Bryan, 2000: Comparison of thermally driven circulations from a depth-coordinate model and an isopycnal-layer model. Part I: Scaling-law sensitivity to vertical diffusivity. *J. Phys. Oceanogr.*, **30**, 590–605, https://doi.org/10.1175/1520-0485(2000)030<0590:COTDCF>2.0.CO;2.

Pedlosky, J., 2003: Thermally driven circulations in small oceanic basins. *J. Phys. Oceanogr.*, **33**, 2333–2340, https://doi.org/10.1175/1520-0485(2003)033<2333:TDCISO>2.0.CO;2.

——, and M. A. Spall, 2005: Boundary intensification of vertical velocity in a β-plane basin. *J. Phys. Oceanogr.*, **35**, 2487–2500, https://doi.org/10.1175/JPO2832.1.

Plumb, R. A., and R. Ferrari, 2005: Transformed Eulerian-mean theory. Part I: Nonquasigeostrophic theory for eddies on a zonal-mean flow. *J. Phys. Oceanogr.*, **35**, 165–174, https://doi.org/10.1175/JPO-2669.1.

Rossby, T., C. Flagg, L. Chafik, B. Harden, and H. Søiland, 2018: A direct estimate of volume, heat, and freshwater exchange across the Greenland-Iceland-Faroe-Scotland ridge. *J. Geophys. Res. Oceans*, **123**, 7139–7153, https://doi.org/10.1029/2018JC014250.

Spall, M. A., 2003: On the thermohaline circulation in flat bottom marginal seas. *J. Mar. Res.*, **61**, 1–25, https://doi.org/10.1357/002224003321586390.

——, 2004: Boundary currents and watermass transformation in marginal seas. *J. Phys. Oceanogr.*, **34**, 1197–1213, https://doi.org/10.1175/1520-0485(2004)034<1197:BCAWTI>2.0.CO;2.

——, 2010: Dynamics of downwelling in an eddy-resolving convective basin. *J. Phys. Oceanogr.*, **40**, 2341–2347, https://doi.org/10.1175/2010JPO4465.1.

——, 2011: On the role of eddies and surface forcing in the heat transport and overturning circulation in marginal seas. *J. Climate*, **24**, 4844–4858, https://doi.org/10.1175/2011JCLI4130.1.

——, and R. S. Pickart, 2001: Where does dense water sink? A subpolar gyre example. *J. Phys. Oceanogr.*, **31**, 810–826, https://doi.org/10.1175/1520-0485(2001)031<0810:WDDWSA>2.0.CO;2.

Stewart, A. L., R. Ferrari, and A. F. Thompson, 2014: On the importance of surface forcing in conceptual models of the deep ocean. *J. Phys. Oceanogr.*, **44**, 891–899, https://doi.org/10.1175/JPO-D-13-0206.1.

Talley, L., 2013: Closure of the global overturning circulation through the Indian, Pacific, and Southern Oceans: Schematics and transports. *Oceanography*, **26**, 80–97, https://doi.org/10.5670/oceanog.2013.07.

Vallis, G. K., 2000: Large-scale circulation and production of stratification: Effects of wind, geometry, and diffusion. *J. Phys. Oceanogr.*, **30**, 933–954, https://doi.org/10.1175/1520-0485(2000)030<0933:LSCAPO>2.0.CO;2.

Wolfe, C. L., and P. Cessi, 2010: What sets the strength of the middepth stratification and overturning circulation in eddying ocean models? *J. Phys. Oceanogr.*, **40**, 1520–1538, https://doi.org/10.1175/2010JPO4393.1.

——, and ——, 2011: The adiabatic pole-to-pole overturning circulation. *J. Phys. Oceanogr.*, **41**, 1795–1810, https://doi.org/10.1175/2011JPO4570.1.

Xu, X., P. B. Rhines, and E. P. Chassignet, 2018: On mapping the diapycnal water mass transformation of the upper North Atlantic Ocean. *J. Phys. Oceanogr.*, **48**, 2233–2258, https://doi.org/10.1175/JPO-D-17-0223.1.

Young, W. R., 2012: An exact thickness-weighted average formulation of the Boussinesq equations. *J. Phys. Oceanogr.*, **42**, 692–707, https://doi.org/10.1175/JPO-D-11-0102.1.

Zhang, S., C. A. Lin, and R. J. Greatbatch, 1992: A thermocline model for ocean-climate studies. *J. Mar. Res.*, **50**, 99–124, https://doi.org/10.1357/002224092784797755.